Research Square

Preprints are preliminary reports that have not undergone peer review.
They should not be considered conclusive, used to inform clinical practice,
or referenced by the media as validated information.

Nd-Doped $NiFe_2O_4$ Nanoparticles for Enhanced X-Band Electromagnetic Wave Absorption

Van Hoanh Ngo
Institute of Materials, Biology and Environment
Thi Hoa Nguyen
Institute of Materials, Biology and Environment
Trung Kien Pham
Institute of Materials, Biology and Environment
Huu Thanh Le
Institute of Materials, Biology and Environment
Duc Duong La
duc.duong.la@gmail.com

Institute of Materials, Biology and Environment

Research Article

Keywords: nickel ferrite, neodymium doping, coercive field, reflection loss, electromagnetic-wave absorption

Posted Date: June 19th, 2026

DOI: https://doi.org/10.21203/rs.3.rs-9957644/v1

License: This work is licensed under a Creative Commons Attribution 4.0 International License.
Read Full License

Additional Declarations: No competing interests reported.

Version of Record: A version of this preprint was published at Journal of Materials Science: Materials in Electronics on August 21st, 2026. See the published version at https://doi.org/10.1007/s10854-026-18311-8.

Abstract

Doping rare-earth (RE) elements into ferrites is an effective strategy for modifying their physical structure, magnetic response, and electromagnetic-wave absorption behavior. In this study, nickel ferrite nanoparticles were modified with a small amount of neodymium (Nd) using a simple coprecipitation method. The influence of Nd content on morphology, crystal structure, elemental composition, magnetic properties, and X-band absorption performance was investigated using SEM-EDX, XRD, EDX mapping, VSM, and vector-network-analyzer measurements. The results confirmed the successful formation of Nd-doped nickel ferrite materials with different Nd contents. Nd incorporation reduced nanoparticle agglomeration and altered the magnetic parameters, particularly saturation magnetization and coercive field, thereby improving impedance matching and electromagnetic-wave attenuation in the 8–12 GHz range. The strongest reflection loss reached − 25.47 dB at 11.56 GHz for the $NiFe_{1.97}Nd_{0.03}O_4$ sample at a matching thickness of 2.0 mm, corresponding to an electromagnetic-wave absorption efficiency of approximately 99.7%. These results indicate that Nd-doped $NiFe_2O_4$ nanoparticles are promising candidates for X-band electromagnetic-wave absorption and shielding applications.

1. Introduction

Electromagnetic waves (EMW) in the X-band frequency range, spanning from 8 to 12 GHz, are commonly emitted by various sources such as weather radar, satellites, and wireless communication devices [1, 2]. These emissions may affect both public health and sensitive electronic equipment. However, achieving adequate electromagnetic absorption within this frequency range remains a challenge because many materials do not simultaneously provide strong reflection loss, broad effective absorption bandwidth (EAB), and suitable impedance matching across the X-band. The primary research goal is to expand the EAB, usually defined as reflection loss below − 10 dB, while maintaining high absorption intensity [3, 4]. To meet these criteria, absorbing materials should possess appropriate impedance matching and strong attenuation ability. A common approach for improving electromagnetic absorption is the construction of magnetic-dielectric synergistic materials [5, 6]. These materials combine dual loss mechanisms and optimized impedance matching to dissipate incident electromagnetic energy [7]. Recent studies have explored magnetic-dielectric composites containing magnetic phases such as ferrites or magnetic nanoparticles [8, 9] and dielectric components such as carbon-based materials or conductive polymers [10, 11].

Nickel ferrite ($NiFe_2O_4$) is well known for its high chemical stability, ferrimagnetic behavior, magnetic anisotropy, and electromagnetic properties, which make it attractive for high-frequency electromagnetic-wave absorption applications [16–18]. These characteristics allow nickel ferrite to exhibit appreciable magnetic response in the GHz range. However, pristine nickel ferrite may suffer from poor impedance matching, particle agglomeration, and limited attenuation pathways, which restrict its microwave absorption performance [14–16]. The dielectric and magnetic properties of nickel ferrite can be modified by controlling its composition, microstructure, particle size, and dopant chemistry. This approach is especially useful for improving EMW absorption within the X-band frequency range [17, 18].

Several studies have investigated changes in the electrical, magnetic, and microwave absorption properties of nickel ferrites induced by rare-earth (RE) ion substitution. RE ions are promising modifiers for spinel ferrites because they possess unpaired 4f electrons and strong spin-orbit coupling [19]. The 4f shells of RE elements are shielded by $5s^2 5p^6$ electrons and are less affected by the surrounding crystal field. Substitution of RE ions into spinel ferrites and the resulting 4f-3d coupling can alter the magnetic anisotropy, coercive field, and microwave absorption behavior of $NiFe_2O_4$ ferrites [20]. In general, increasing the RE ion substitution level may increase coercivity while decreasing saturation magnetization, depending on the dopant concentration, particle size, cation distribution, and secondary-phase formation. In the present work, nickel ferrite was substituted with neodymium (Nd^{3+}) in the nominal composition $NiFe_{2-x}Nd_xO_4$ using a coprecipitation route. The effects of Nd substitution on the structural, magnetic, and X-band microwave absorption properties of $NiFe_2O_4$ were systematically examined [21, 22].

In this study, a facile coprecipitation approach was employed to synthesize Nd-doped nickel ferrite nanoparticles with controlled composition and enhanced electromagnetic properties. Unlike previous studies that mainly focused on bulk magnetic enhancement, this work correlates Nd-induced microstructural modification, including reduced agglomeration, increased porosity, and nanoscale particle refinement, with improved magnetic parameters and X-band microwave absorption behavior. The introduction of a low Nd doping level effectively tuned the saturation magnetization and coercive field while maintaining the spinel ferrite structure, leading to enhanced reflection loss. The calculation basis for magnetic parameters and electromagnetic absorption performance is clarified to support quantitative interpretation of the results.

2. Materials and methods

2.1. Materials

Nickel nitrate hexahydrate ($Ni(NO_3)_2 \cdot 6H_2O$, Aladdin Reagent, 99%), iron nitrate nonahydrate ($Fe(NO_3)_3 \cdot 9H_2O$, E. Merck, 98%), neodymium(III) nitrate hexahydrate ($Nd(NO_3)_3 \cdot 6H_2O$), and citric acid monohydrate (Aladdin Reagent, 99%) were used as starting chemicals.

Nickel(II) nitrate, iron(III) nitrate, and neodymium(III) nitrate with a molar ratio of 1:(2-x):x, corresponding to the nominal formula $NiFe_{2-x}Nd_xO_4$, were separately dissolved in 30 mL of water under magnetic stirring to form homogeneous solutions. A solution containing 1 mmol citric acid was added to the $Ni(NO_3)_2 \cdot 6H_2O$ solution. Subsequently, this solution was mixed with $Fe(NO_3)_3 \cdot 9H_2O$ and $Nd(NO_3)_3 \cdot 6H_2O$ solutions. The final mixed solution was continuously stirred at 80°C to form a gel. The as-synthesized powder was dried in air at 100°C for 24 h and calcined at 800°C for 4 h. After thermal treatment, the system was allowed to cool naturally to room temperature, and the obtained powder was collected for characterization.

2.2. Materials characterization

The surface morphology and elemental composition were examined using a scanning electron microscope (Hitachi S-4800) equipped with energy-dispersive X-ray spectroscopy at an accelerating voltage of 15 kV (SEM-EDX). The crystal structures of the materials were determined using a Bruker D8-Advance X-ray diffractometer with Cu Kα radiation over a 2θ range of 10–70°. Raman spectra were recorded using a LabRam HR Evolution Raman microscope with 532 nm laser excitation. Static magnetic properties were measured using a vibrating sample magnetometer (VSM, DMS880). Saturation magnetization (M□) was obtained from the high-field region of the M-H hysteresis loop, while the coercive field (Hc) was determined from the magnetic field value at which magnetization crossed zero. Therefore, the parameter H reported in this manuscript refers to coercive field (Hc, Oe), not complex permeability.

The electromagnetic-wave absorption performance was evaluated using a Keysight N9918A vector network analyzer in the X-band frequency range of 8–12 GHz. The reflection loss was calculated from the measured reflection coefficient according to RL(dB) = 20 $\log_{10}|S_{11}|$. The absorption efficiency was estimated from the reflected power as Absorption (%) = [1–10^(RL/10)] × 100, assuming negligible transmission through the backed absorber. For the impedance-matching interpretation, the input impedance of a single-layer absorber can be expressed as Zin = Z0(μr/εr)^1/2 tanh[j(2πfd/c)(μrεr)^1/2], and RL = 20 $\log_{10}|(Zin - Z0)/(Zin + Z0)|$, where Z0 is the impedance of free space, μr and εr are the relative complex permeability and permittivity, f is frequency, c is the velocity of light, and d is the absorber thickness. The reflection-loss curves and the maximum RL values reported here correspond to a fixed matching thickness of 2.0 mm.

3. Results and discussion

The surface structures of the material samples were investigated by SEM, which provided detailed information on their microstructure (Fig. 1). The analysis revealed significant variations in texture and porosity, indicating that Nd doping influenced the particle growth and aggregation behavior.

The pristine nickel ferrite surface was relatively compact, with fewer pores and voids, mainly due to ferrite particle aggregation. After Nd doping, the surface morphology became more porous, indicating an increase in accessible surface area. The samples with x = 0.03 and 0.04 showed better dispersion, and rounded grains with sizes of approximately 30–60 nm could be identified. The morphology more clearly revealed magnetic nanoparticles after Nd incorporation. The improved dispersion and reduced agglomeration of nickel ferrite nanoparticles after rare-earth doping are consistent with related studies on substituted spinel ferrites.

Nd^{3+} ions located near grain boundaries can inhibit grain growth and increase lattice strain. Owing to their larger ionic radius compared with Fe^{3+} ions, Nd^{3+} ions are less likely to fully occupy tetrahedral or octahedral sites and may partially segregate at grain boundaries or induce secondary-phase formation. The large ionic-size mismatch between Nd^{3+} and Fe^{3+} can cause lattice distortion, affecting lattice alignment near grain boundaries and thereby modifying the structural and magnetic properties [20].

The chemical composition of the synthesized materials was systematically analyzed using EDX spectroscopy (Fig. 2) and EDX mapping (Fig. 3), with quantitative data summarized in Table 1. The pristine $NiFe_2O_4$ sample contained O, Fe, and Ni with mass percentages of 26.88%, 56.63%, and 16.49%, respectively, indicating the absence of detectable impurities. Upon Nd doping at x = 0.01, 0.02, 0.03, and 0.04, the Nd content progressively increased to 0.72%, 1.63%, 2.75%, and 3.43%, respectively. This trend demonstrates effective control of dopant incorporation during synthesis. EDX mapping further showed a relatively uniform Nd distribution within the ferrite matrix, supporting successful integration of Nd-containing species into the material system. These results provide strong evidence for the incorporation of neodymium into the $NiFe_2O_4$-based structure, which is essential for tailoring its magnetic and electromagnetic properties.

Table 1
Elemental contents of Nd-doped nickel ferrite.

Sample	O (wt%)	Fe (wt%)	Ni (wt%)	Nd (wt%)
$NiFe_2O_4$	26.88	56.63	16.49	0
$NiFe_{1.99}Nd_{0.01}O_4$	33.41	47.45	18.42	0.72
$NiFe_{1.98}Nd_{0.02}O_4$	33.91	48.42	16.04	1.63
$NiFe_{1.97}Nd_{0.03}O_4$	27.76	52.85	16.65	2.75
$NiFe_{1.96}Nd_{0.04}O_4$	25.87	52.01	18.68	3.43

X-ray diffraction patterns were used to examine the crystal structure of the samples (Fig. 4). The XRD pattern of $NiFe_2O_4$ showed diffraction peaks at 2θ values of 18.4°, 30.3°, 35.7°, 43.4°, 54.0°, 57.5°, and 63.1°, corresponding to the (111), (220), (311), (400), (422), (511), and (440) planes of spinel $NiFe_2O_4$ (JCPDS card No. 01-087-2267). For the $NiFe_{2-x}Nd_xO_4$ samples, the XRD patterns displayed not only the characteristic peaks of nickel ferrite but also weak peaks related to Nd-containing secondary oxide phases at 2θ values of approximately 24.3° and 33.2°. The intensity of these Nd-related peaks increased with increasing Nd content, indicating the formation of a small amount of secondary phase at higher dopant levels. In addition, the main (311) peak shifted slightly from 2θ = 35.56° for pristine $NiFe_2O_4$ to 2θ = 35.75° for the Nd-doped sample, suggesting lattice distortion caused by Nd incorporation and/or grain-boundary segregation.

The larger ionic radius of Nd^{3+} compared with Fe^{3+} can induce lattice distortion and modify the position of the characteristic (311) reflection. When Nd ions are introduced into the $NiFe_2O_4$ structure, partial substitution and secondary-phase formation may occur, resulting in distinct Nd-containing oxide reflections. This phenomenon can be identified through the evolution of XRD peak positions and intensities [20].

The effect of Nd doping content on magnetic properties was investigated using VSM hysteresis loops (Fig. 5). As described in the experimental section, M□ was determined from the high-field magnetization,

whereas Hc was obtained from the field-axis intercept of the hysteresis loop. With increasing Nd content, the coercive field (Hc, Oe) generally increased, whereas the saturation magnetization (M_s, emu g^{-1}) tended to decrease. Pristine $NiFe_2O_4$ exhibited an M_s value of 33.05 emu g^{-1}, which decreased to 27.65 emu g^{-1} for the $NiFe_{1.96}Nd_{0.04}O_4$ sample. In contrast, Hc increased from 10577 Oe for pristine $NiFe_2O_4$ to 10801 Oe for $NiFe_{1.97}Nd_{0.03}O_4$. At Nd contents of x = 0.03 and 0.04, the changes in magnetic parameters became less pronounced, suggesting that an Nd content near x = 0.03 is sufficient to modify the magnetic response of $NiFe_2O_4$.

The decrease in M_s can be attributed to the substitution of magnetic Fe^{3+} ions by Nd^{3+} ions and to the weakening of A-B superexchange interactions within the spinel lattice. The coercive field is related to domain-wall pinning and is influenced by microstrain, magnetocrystalline anisotropy, magnetic particle morphology, domain size, and particle-size distribution [20]. The increase in Hc with Nd content can be explained by increased lattice distortion, reduced structural symmetry, and enhanced magnetocrystalline anisotropy. In addition, decreasing crystallite and particle size increases the fraction of disordered ions near grain boundaries, which can hinder domain-wall motion and increase coercivity [19, 20].

The electromagnetic-wave absorption capabilities of the materials are illustrated in Fig. 6 and summarized in Table 2. All samples exhibited measurable absorption in the 8–12 GHz frequency range. With increasing Nd content, the absorption performance generally improved, reaching a maximum absorption efficiency of 99.7% for the $NiFe_{1.97}Nd_{0.03}O_4$ sample, corresponding to a reflection loss of -25.47 dB at 11.56 GHz and a matching thickness of 2.0 mm. The maximum absorption peak tended to shift toward lower frequency with increasing Nd content. This trend is consistent with the magnetic results, where the increased Hc and modified M_s suggest stronger magnetic anisotropy and improved electromagnetic attenuation. The $NiFe_{1.97}Nd_{0.03}O_4$ sample showed the best combination of magnetic response and reflection-loss performance. These results indicate that Nd-doped nickel ferrite nanoparticles are promising candidates for electromagnetic-wave absorption and shielding applications in the X-band. Further work should include complex permittivity/permeability measurements and thickness-dependent simulations to clarify the detailed impedance-matching mechanism.

Table 2
Reflection loss and microwave absorption values of Nd-doped nickel ferrite samples.

Sample	Frequency (GHz)	Matching thickness (mm)	Reflection loss (dB)	Microwave absorption (%)
$NiFe_2O_4$	11.82	2.0	-13.02	95.0
$NiFe_{1.99}Nd_{0.01}O_4$	11.54	2.0	-16.14	97.6
$NiFe_{1.98}Nd_{0.02}O_4$	11.32	2.0	-18.14	98.5
$NiFe_{1.97}Nd_{0.03}O_4$	11.56	2.0	-25.47	99.7
$NiFe_{1.96}Nd_{0.04}O_4$	11.56	2.0	-20.56	99.1

4. Conclusion

Neodymium-modified nickel ferrite nanoparticles were successfully synthesized via a coprecipitation method and showed improved structural, magnetic, and electromagnetic-wave absorption properties. Incorporation of a small amount of Nd reduced agglomeration, refined the particle morphology, and increased porosity, contributing to better dispersion and surface interaction. XRD analysis confirmed the formation of the spinel $NiFe_2O_4$ phase with Nd-induced lattice distortion and minor Nd-containing secondary phases. The magnetic behavior was modified by Nd doping: M□ decreased from 33.05 emu g^{-1} for pristine $NiFe_2O_4$ to 27.65 emu g^{-1} for $NiFe_{1.96}Nd_{0.04}O_4$, while Hc increased from 10577 Oe to 10801 Oe for $NiFe_{1.97}Nd_{0.03}O_4$. The optimized $NiFe_{1.97}Nd_{0.03}O_4$ sample exhibited the best X-band microwave absorption performance, with a maximum reflection loss of -25.47 dB at 11.56 GHz and a matching thickness of 2.0 mm, corresponding to approximately 99.7% absorption. These results demonstrate that Nd-modified $NiFe_2O_4$ nanoparticles are promising candidates for electromagnetic-wave absorption and shielding materials.

Declarations

CRediT authorship contribution statement

Van Hoanh Ngo and Huu Thanh Le: Funding acquisition, writing-review and editing. Thi Hoa Nguyen and Trung Kien Pham: Data curation. Duc Duong La: Investigation, writing-original draft, and validation.

Declaration of competing interest

The authors declare that they have no known competing financial interests or personal relationships that could have appeared to influence the work reported in this paper.

Data Availability

Data will be made available on request.

Acknowledgement

This research was funded by Science and Technology Development Project Number 10/2025/HĐKHCN.

References

1. M. Harmouzi, B. Sebbar, M.E. Hadri, M.A. Ennasar, B. Mohamed, (2025) Int. J. Microw. Opt. Technol. 20
2. PR Hoole, *Smart antennas and electromagnetic signal processing in advanced wireless technology* (River, 2022)
3. Y. Shi, B. Liang, H. Gao et al., Carbon. **227**, 119244 (2024)
4. Z.-L. Hou, X. Gao, J. Zhang, G. Wang, Carbon. **222**, 118935 (2024)

5. L. Wang, X. Li, X. Shi et al., Nanoscale. **13**, 2136 (2021)
6. C. Shao, H. Liu, Y. Shi, N. Tian, C. You, Z. Zhao, (2025) Nano Res. 18
7. H. Wang, H. Zhang, K. Zhao et al., Adv. Composit Hybrid. Mater. **6**, 120 (2023)
8. X. Chen, D. Lan, L. Zhou et al., Int. J. Min. Metall. Mater. **32**, 591 (2025)
9. Y. Wei, S. Dong, S. Mehrez, M.N. Akhtar, HT Giang, Ceram. Int. **48**, 25049 (2022)
10. R. Shu, K. Yun, X. Liu, L. Xu, Compos. Part A Appl. Sci. Manuf. **188**, 108558 (2025)
11. C. Liu, J. Lin, N. Wu et al., Carbon. **223**, 119017 (2024)
12. M. Khairy, (2014) Synth. Met. 189: 34
13. A. Alarifi, N. Deraz, S. Shaban, J. Alloys Compd. **486**, 501 (2009)
14. Z. Tong, Q. Yao, J. Deng et al., Mater. Sci. Eng. B **268**, 115092 (2021)
15. Z. Yan, J Luo, J. Alloys Compd. **695**, 1185 (2017)
16. A.A. Ati, Z. Othaman, A. Samavati, J. Mol. Struct. **1052**, 177 (2013)
17. M. Bala, V. Shivling, S. Tyagi, Mater. Chem. Phys. **312**, 128630 (2024)
18. M. Bala, V. Shivling, S. Tyagi, Ceram. Int. **50**, 34123 (2024)
19. S.H. Yunasfi, M. Dewi, D.S. Mashadi, J. Winatapura, A. Setiawan, Y.E. Mulyawan, W.A. Gunanto, Adi, J. Magn. Magn. Mater. **603**, 172267 (2024). 10.1016/j.jmmm.2024.172267
20. J. Setiawan, M. Mashadi, D.S. Winatapura, Y. Taryana, N. Sudrajat, W.A. Yunasfi, Adi, J. Magn. Magn. Mater. **563**, 170023 (2022). 10.1016/j.jmmm.2022.170023
21. A. Nikzad, R. Parvizi, J. Rare Earths. **38**, 411 (2020)
22. F.R. Mariosi, J. Venturini, A. Cas, C.P. Viegas Bergmann, Ceram. Int. **46**, 2772 (2020)

Figures

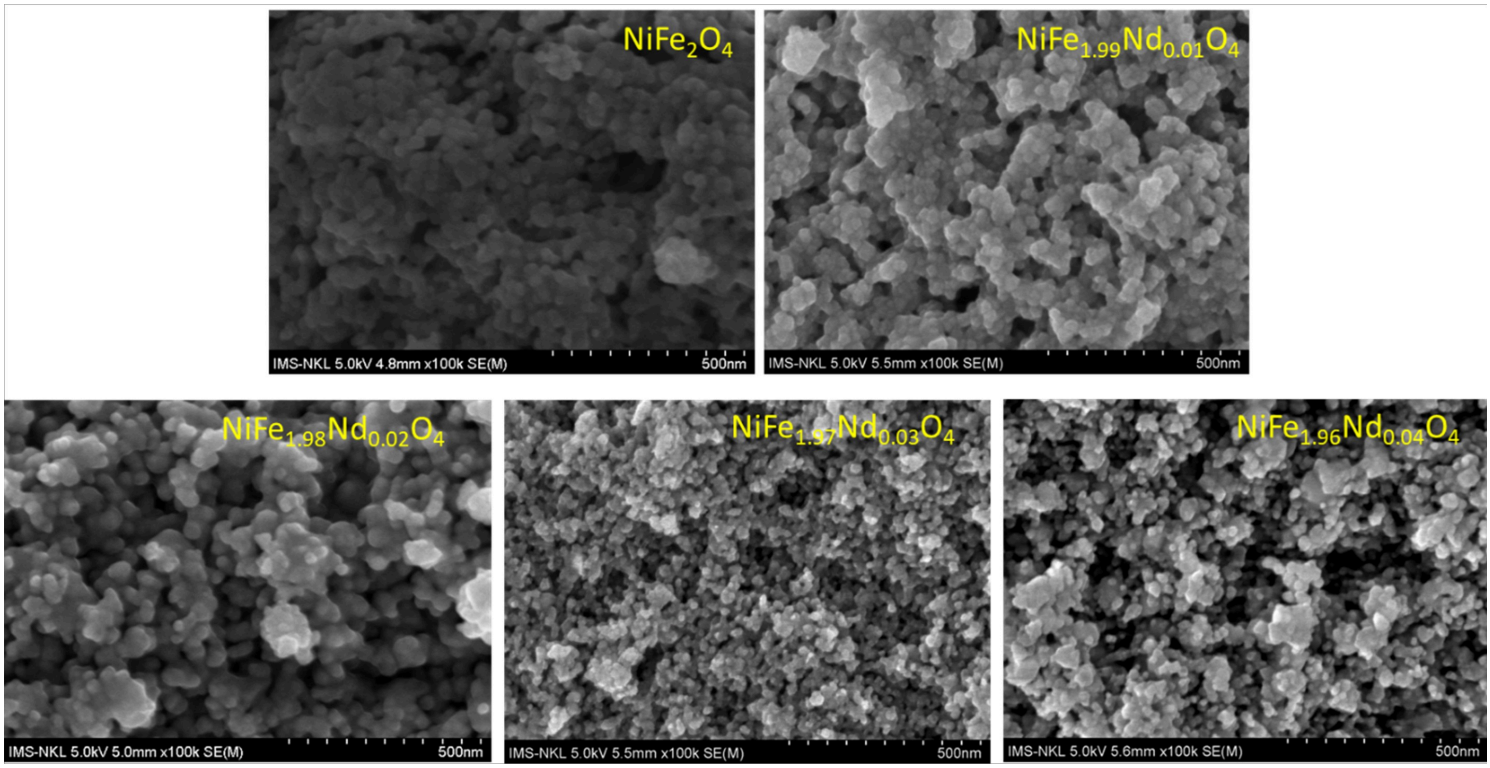


Figure 1

SEM images of Nd-doped nickel ferrite with different Nd contents.

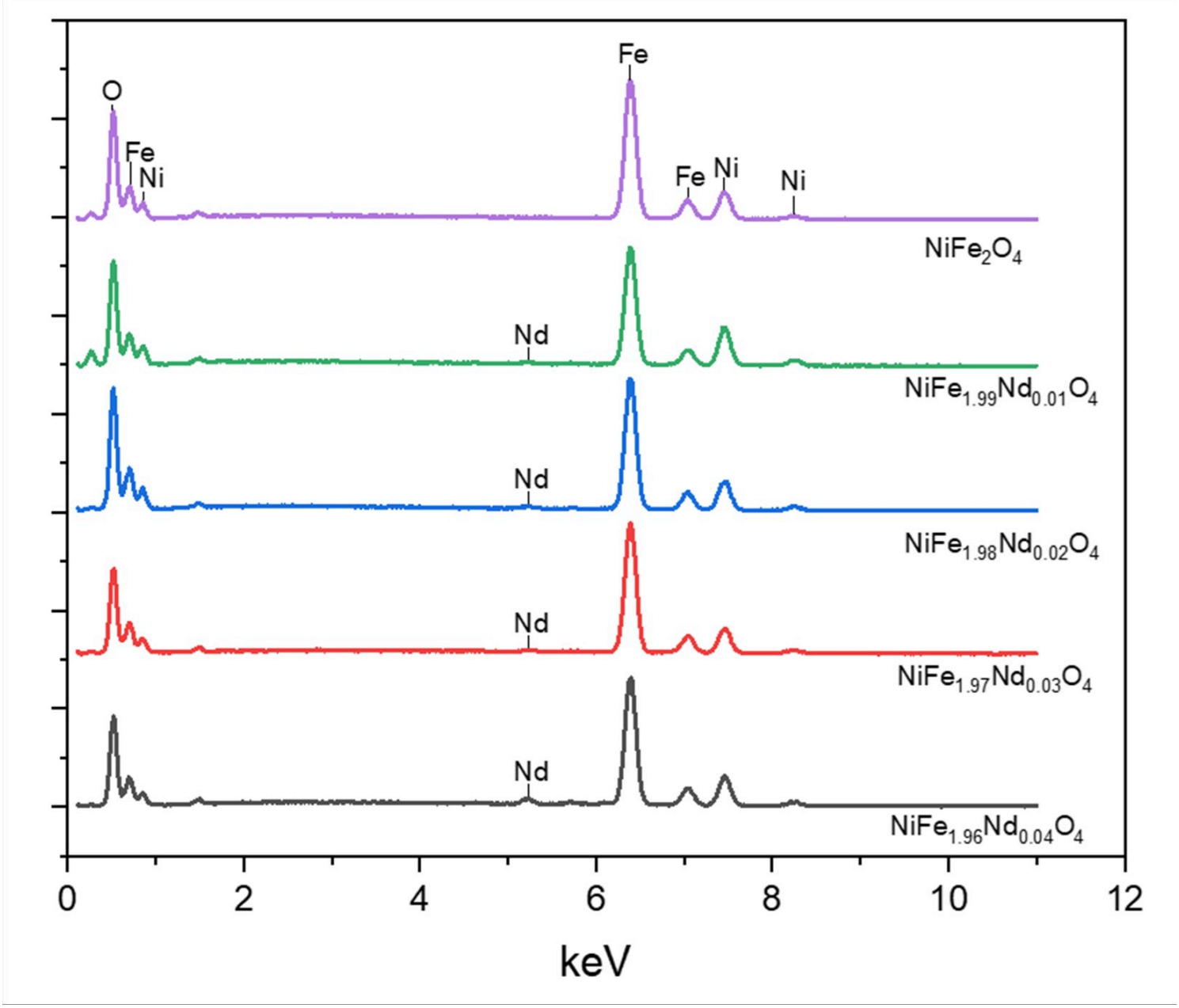


Figure 2

EDX spectra of Nd-doped nickel ferrite.

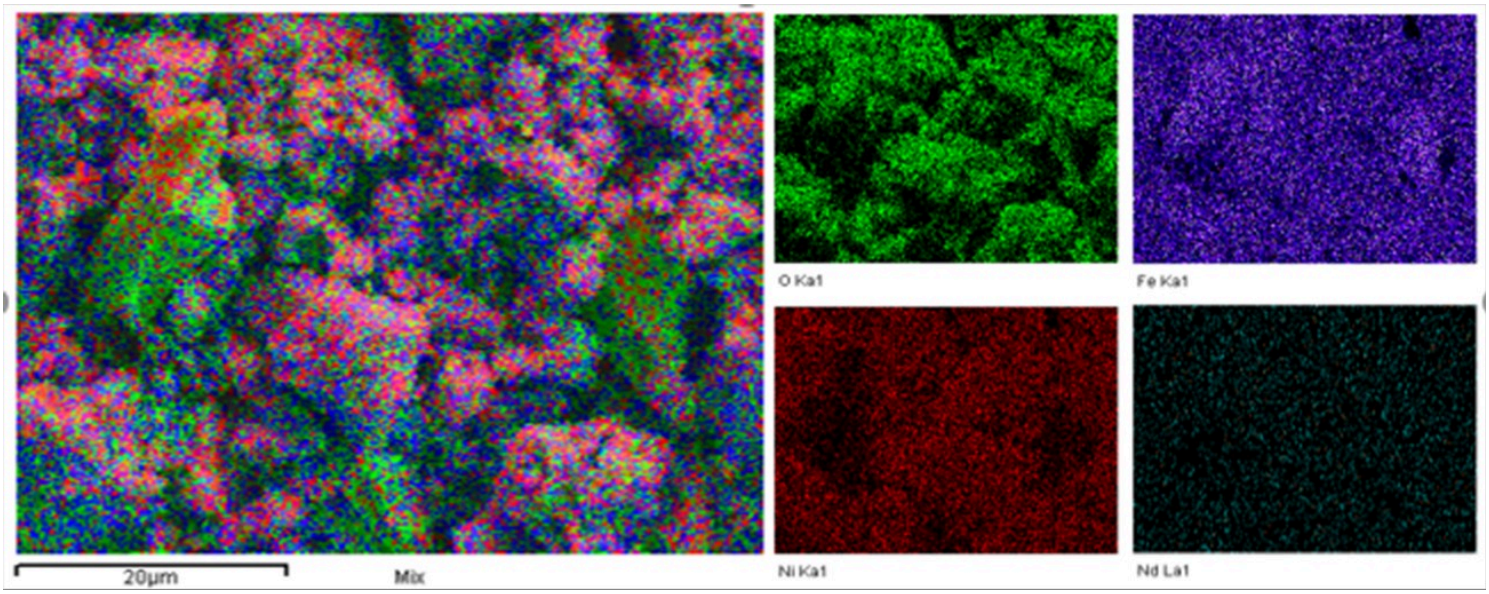


Figure 3

EDX mapping of Nd-doped nickel ferrite.

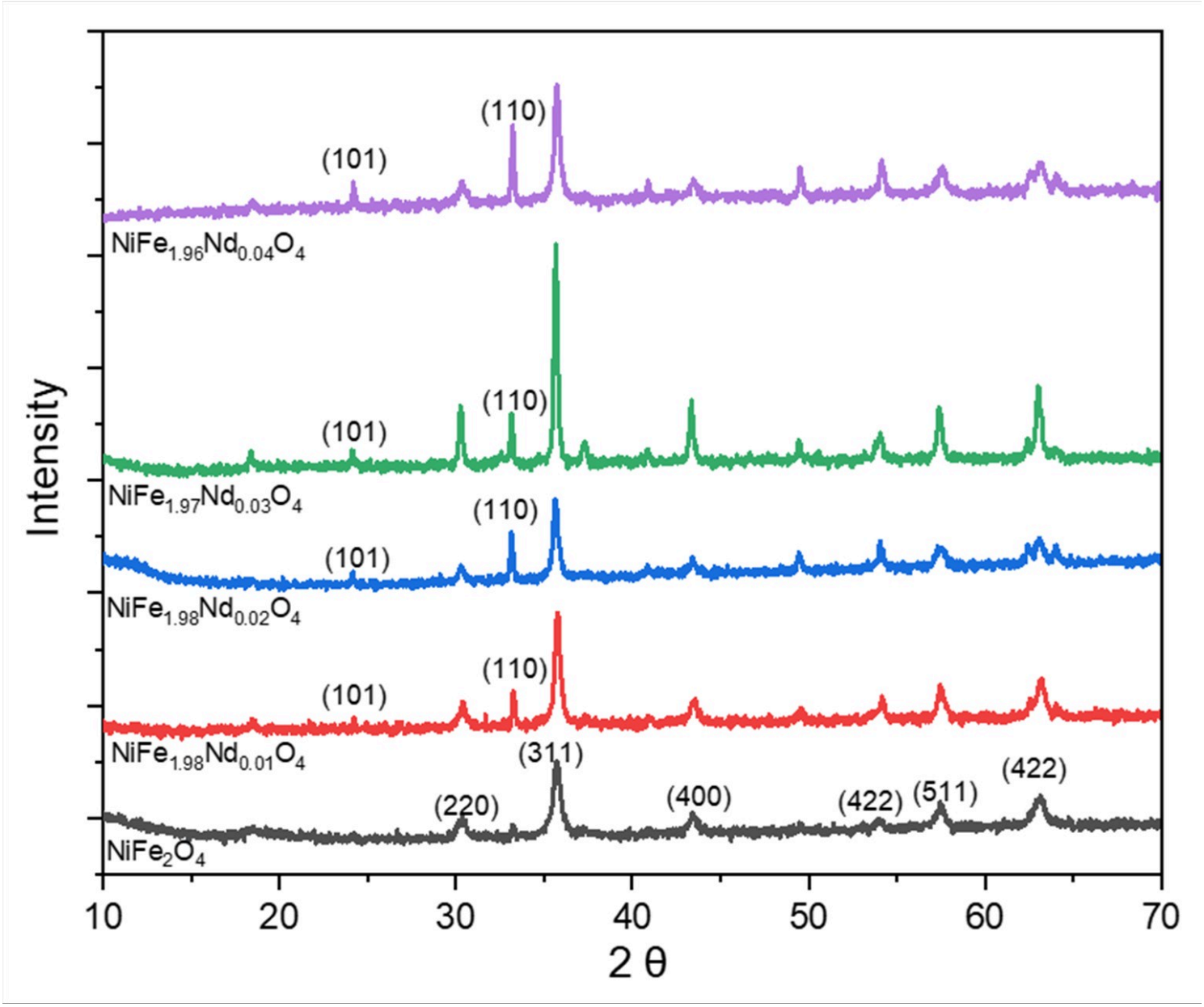


Figure 4

XRD patterns of Nd-doped nickel ferrite.

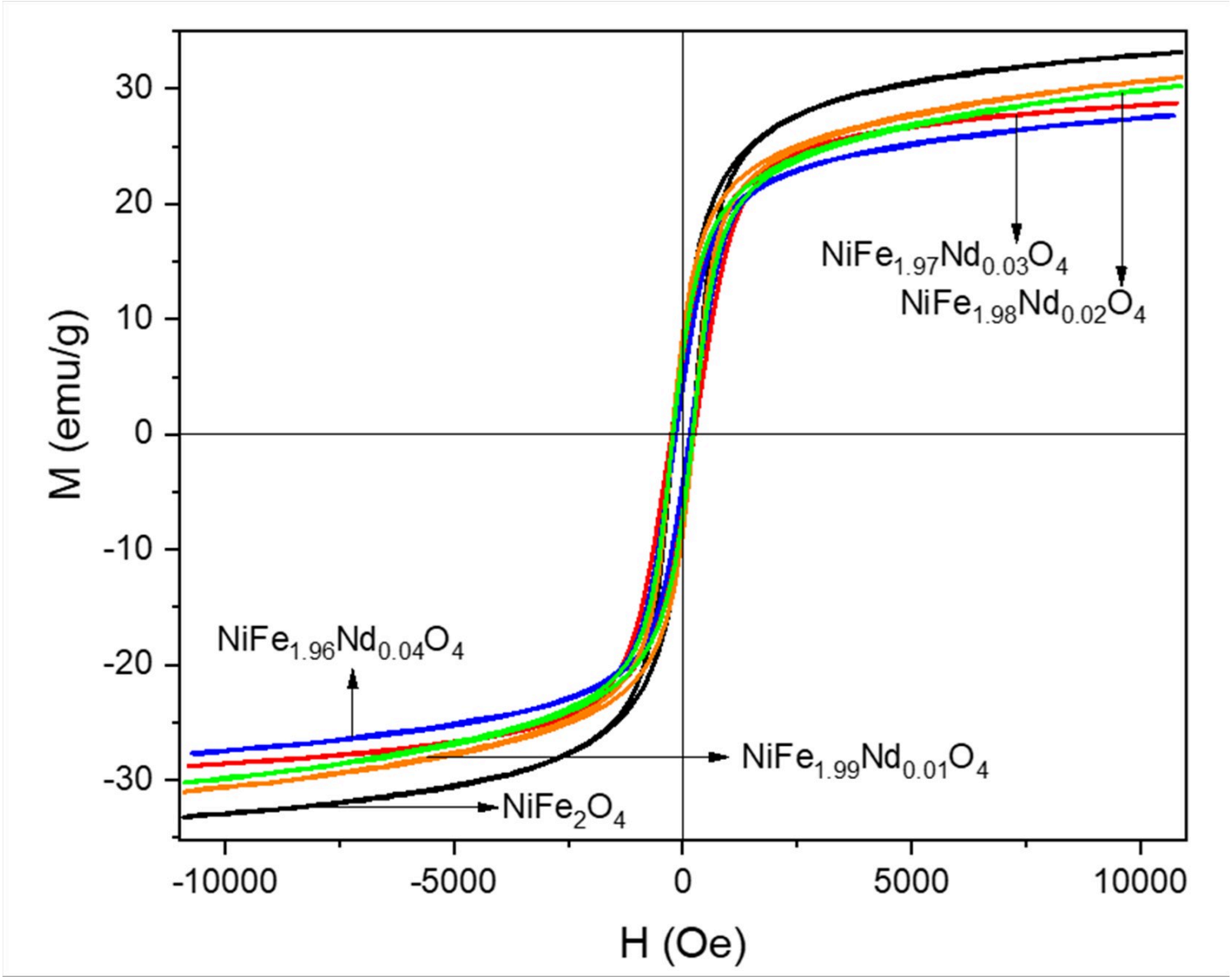


Figure 5

Hysteresis loops of Nd-doped nickel ferrite.

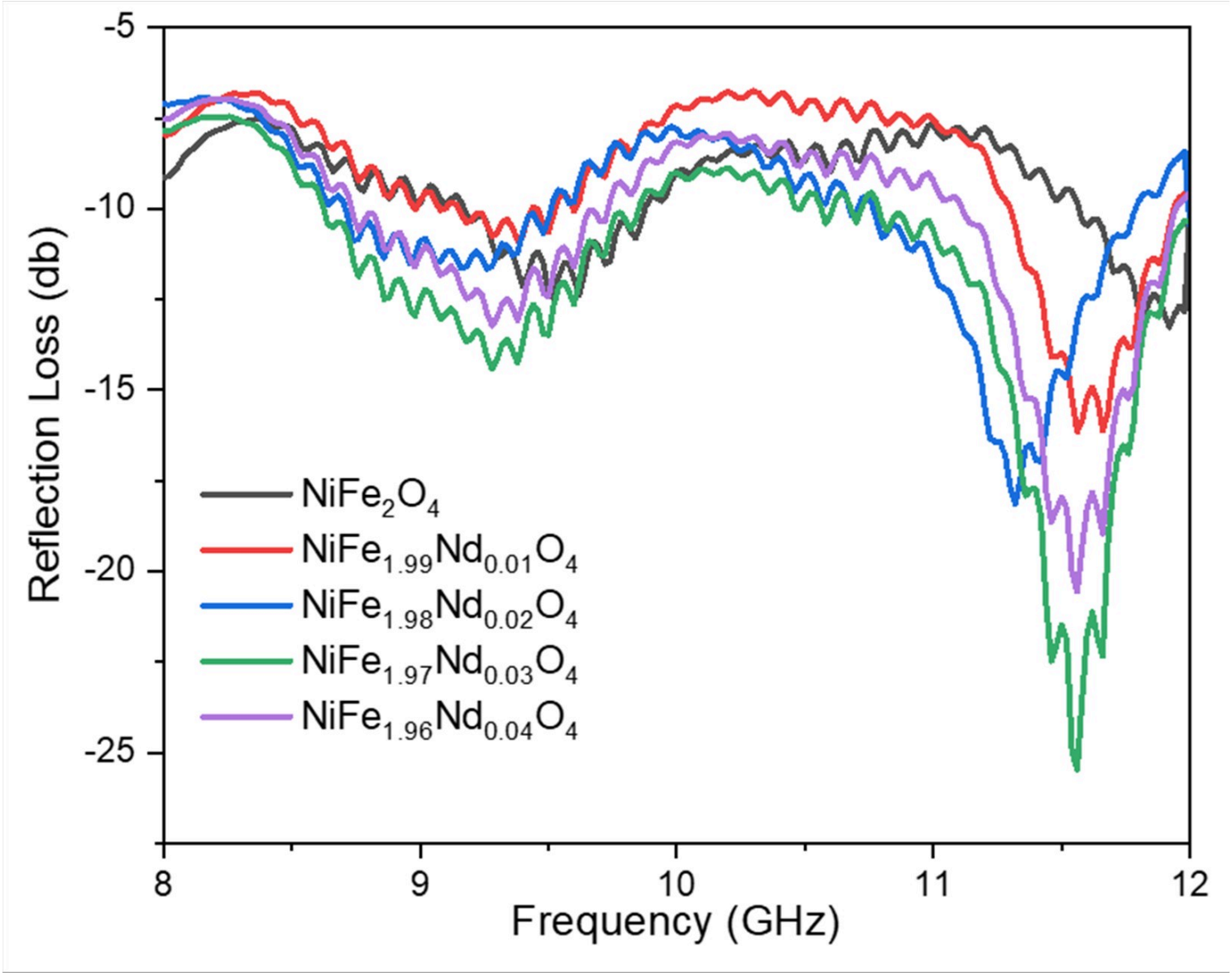


Figure 6

Reflection loss curves of Nd-doped nickel ferrite.